Supplemental Information

Independent and coherent transitions between antiferromagnetic states of few-molecule systems

Claire Besson, Philipp Stegmann, Michael Schnee, Zeila Zanolli, Simona Achilli, Nils Wittemeier, Asmus Vierck, Robert Frielinghaus, Paul Kögerler, Janina Maultzsch, Pablo Ordejón, Claus M. Schneider, Alfred Hucht, Jürgen König, Carola Meyer*

*Correspondence should be addressed to carola.meyer@uos.de

SI-1 Discussion of spin states in the {M₄} complex

In our effective spin model, we use the fact that each of the four Mn^{II} ions, $i = 1, \cdots, 4$ carries a spin $\vec{S}_i$ with spin quantum number $S_i = \frac{5}{2}$, and magnetic quantum number $S_i^z = -\frac{5}{2}, -\frac{3}{2}, \cdots, \frac{5}{2}$. This yields a 6^4-dimensional Hilbert space for the spin states. Instead of characterizing the spin states by the quantum numbers $\{S_1^z, S_2^z, S_3^z, S_4^z\}$, we can use the standard procedure for adding angular momenta to find a basis that is more convenient for our purpose. Let S_{ij} be the spin quantum number and S_{ij}^z be the magnetic quantum number of the spin sum $\vec{S}_{ij} := \vec{S}_i + \vec{S}_j$. In a first step, we combine spins 1 with 2 and 3 with 4 (see Fig. S1). This leads to a new basis characterised by $\{S_{12}, S_{12}^z, S_{34}, S_{34}^z\}$. In a second step, we form the total spin

$$\vec{S}_{\text{tot}} := \sum_{i=1}^{4} \vec{S}_i = \vec{S}_{12} + \vec{S}_{34} \tag{1}$$

with the spin quantum number S_{tot} and the magnetic quantum number S_{tot}^z. The resulting basis can be labelled by the set of quantum numbers $\{S_{\text{tot}}, S_{\text{tot}}^z, S_{12}, S_{34}\}$. (Alternatively, we could have chosen $\{S_{\text{tot}}, S_{\text{tot}}^z, S_{13}, S_{24}\}$ or $\{S_{\text{tot}}, S_{\text{tot}}^z, S_{14}, S_{23}\}$.)
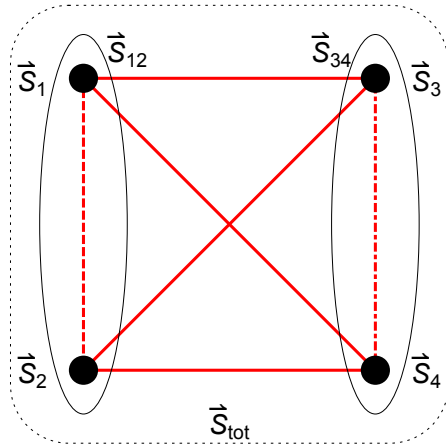

Figure S1 | Schematic view of the spin system of the {Mn₄} complex. Four $\frac{5}{2}$ - spins are coupled to each other. If all exchange interactions are equal, the ground state is six-fold degenerate. For small deviations between the interactions, the degeneracy is split into six antiferromagnetic eigenstates of different energy.

We assume a Heisenberg-like spin-exchange coupling for each pair of Mn spins,

$$H = -\frac{1}{2} \sum_{i \neq j} J_{ij} \vec{S}_i \cdot \vec{S}_j \tag{2}$$

with antiferromagnetic $J_{ij} < 0$.

If all exchange couplings are equal, $J_{ij} = J$, we can use $\sum_{i \neq j} \vec{S}_i \cdot \vec{S}_j = \vec{S}_{\text{tot}}^2 - \sum_i \vec{S}_i^2$, together with $\vec{S}_{\text{tot}}^2 = S_{\text{tot}}(S_{\text{tot}} + 1)$ and $\vec{S}_i^2 = S_i(S_i + 1) = \frac{35}{4}$ to see that the eigenenergy

$$E = -\frac{J}{2}[S_{\text{tot}}(S_{\text{tot}} + 1) - 35] \tag{3}$$

only depends on the spin quantum number S_{tot} of the total spin but not on S_{tot}^z, S_{12}, or S_{34}. For antiferromagnetic coupling, $J < 0$, the ground state has total spin $S_{\text{tot}} = 0$ with vanishing dipole moment, $S_{\text{tot}}^z = 0$. It is six-fold degenerate with

$$|S_{\text{tot}}, S_{\text{tot}}^z, S_{12}, S_{34}\rangle = |0,0,0,0\rangle, |0,0,1,1\rangle, |0,0,2,2\rangle, |0,0,3,3\rangle, |0,0,4,4\rangle, |0,0,5,5\rangle$$

Unequal J_{ij}'s remove this degeneracy. Instead of a six-fold degenerate ground state, there are now six energy eigenstates, all with $S_{\text{tot}} = S_{\text{tot}}^z = 0$, as long as the variation between the different J_{ij}'s is not too large. States with $S_{\text{tot}} > 0$ remain higher in energy. Therefore, we can conclude that both the ground and the first excited state do not carry any dipole moment, i.e. $S_{\text{tot}}^z = 0$.

As an example, assuming $J_{12} < J_{34} < J_{31} = J_{14} = J_{23} = J_{24}$ the ground state $|\Psi_0\rangle = |0,0,0,0\rangle$ and the first excited state $|\Psi_1\rangle = |0,0,1,1\rangle$ (in the S^z-base) are given by:

Ground state:

$$|\Psi_0\rangle = |\varphi_0\rangle \otimes |\varphi_0\rangle \text{ with}$$

$$|\varphi_0\rangle = \frac{1}{\sqrt{6}} \left(\left|\tfrac{5}{2}, -\tfrac{5}{2}\right\rangle - \left|\tfrac{3}{2}, -\tfrac{3}{2}\right\rangle + \left|\tfrac{1}{2}, -\tfrac{1}{2}\right\rangle - \left|-\tfrac{1}{2}, \tfrac{1}{2}\right\rangle + \left|-\tfrac{3}{2}, \tfrac{3}{2}\right\rangle - \left|-\tfrac{5}{2}, \tfrac{5}{2}\right\rangle \right).$$

First excited state:

$$|\Psi_1\rangle = a_{-1}|\varphi_{1,-1}\rangle \otimes |\varphi_{1,1}\rangle - a_0|\varphi_{1,0}\rangle \otimes |\varphi_{1,0}\rangle + a_1|\varphi_{1,1}\rangle \otimes |\varphi_{1,-1}\rangle \text{ with}$$

$$|\varphi_{1,1}\rangle = \frac{\sqrt{10}\left|+\tfrac{5}{2}, -\tfrac{3}{2}\right\rangle - 4\left|+\tfrac{3}{2}, -\tfrac{1}{2}\right\rangle + 3\sqrt{2}\left|+\tfrac{1}{2}, +\tfrac{1}{2}\right\rangle - 4\left|-\tfrac{1}{2}, +\tfrac{3}{2}\right\rangle + \sqrt{10}\left|-\tfrac{3}{2}, +\tfrac{5}{2}\right\rangle}{\sqrt{70}},$$

$$|\varphi_{1,0}\rangle = \frac{5\left|+\tfrac{5}{2}, -\tfrac{5}{2}\right\rangle - 3\left|+\tfrac{3}{2}, -\tfrac{3}{2}\right\rangle + \left|+\tfrac{1}{2}, -\tfrac{1}{2}\right\rangle + \left|-\tfrac{1}{2}, +\tfrac{1}{2}\right\rangle - 3\left|-\tfrac{3}{2}, +\tfrac{3}{2}\right\rangle + 5\left|-\tfrac{5}{2}, +\tfrac{5}{2}\right\rangle}{\sqrt{70}},$$

$$|\varphi_{1,-1}\rangle = \frac{\sqrt{10}\left|+\tfrac{3}{2}, -\tfrac{5}{2}\right\rangle - 4\left|+\tfrac{1}{2}, -\tfrac{3}{2}\right\rangle + 3\sqrt{2}\left|-\tfrac{1}{2}, -\tfrac{1}{2}\right\rangle - 4\left|-\tfrac{3}{2}, +\tfrac{1}{2}\right\rangle + \sqrt{10}\left|-\tfrac{5}{2}, +\tfrac{3}{2}\right\rangle}{\sqrt{70}}.$$

The coefficients verify $a_i = \frac{1}{\sqrt{3}}$ for magnetic field $B = 0$. They differ in case a magnetic field is applied.

The same procedure applies to M = Co, except for the difference in spin quantum number, which is only 3/2 for Co^{II}, so that the singlet ground state is only 4-fold (instead of 6-fold) degenerate in the case of a perfect magnetic tetrahedron. Again, the degeneracy between those states is lifted as the J couplings between centers are not identical in the actual complex.

SI-2 DFT calculations of {Mn4} and {Co4} complex grafted to the carbon nanotube.

The structural, electronic and magnetic properties of the **{M4}**-CNT hybrid systems (where M = Mn or Co) are computed from first principles using the SIESTA[1-2] code. The **{M4}** complex is bound via a -CO_2^- group to the dangling C of a mono-vacancy site on the external wall of a metallic armchair (5, 5) nanotube. The choice of a metallic nanotube ensures that electron conduction is allowed around the Fermi energy. Previous studies have demonstrated that the mono-vacancy site is especially favorable for functionalization of CNTs with molecules[3] or magnetic nanoparticles.[4]

In order to take into account the strong correlation of the 3d electrons and avoid the excessive delocalisation of the *d* states predicted in the Local Density Approximation, Hubbard-like corrections $U = 6$ eV and $U = 4$ eV were used for Mn and Co, respectively (LDA+U method).[5] The same $U = 6$ eV value was used by Kampert *et al.* in their calculations on **{Mn4}**.[6] A standard double zeta polarised (DZP) basis set was used for carbon, nitrogen and hydrogen, and an optimised double-zeta (DZ) for Mn, Co and O. Calculations were spin polarised and performed assuming collinear spins. LDA+SOC calculations (off-site formalism of Ref. [7]) without Hubbard correction were performed in order to determine the orbital moments and the role of SOC as currently, the SIESTA code does not allow to include both SOC and Hubbard correction. We verified that the effect of spin-orbit interaction is negligible in **{Mn4}** (as expected for a half filled *3d* shell) but not in **{Co4}**. Convergence of electronic structure and magnetic properties was achieved for a real space grid cut-off of 400 Ry, and a Fermi-Dirac smearing of 100 K in the LDA+U calculation, while with SOC a cut-off of 650 Ry and electronic temperature of 1 K were adopted. The atomic positions were relaxed in standard periodic boundary conditions simulations, with a $1 \times 1 \times 12$ k-points sampling of the Brillouin zone for 15 cells of **{M4}**-CNT (shifted grid), and the conjugate gradient algorithm. The simulation cell extends for 36.9354 Å (30 carbon atoms) along the periodic direction while more than 30 Å of vacuum between periodic replica of the system have been taken in the two directions perpendicular to the tube axis. The maximum force on atoms was smaller than 0.04 eV/Å for the CNT+**{M4}** system. Open-system simulations were performed within a non-equilibrium Green's function formalism, using the TranSIESTA solution method,[8-9] on a 70-carbons long units consisting of the relaxed {M4-CNT} unit padded with (5,5)-CNT fragments (20 carbons long total) on either side.

1) Periodic boundary condition simulations

a) {M4}-CNT ground state magnetic configuration

Collinear-spin PBC simulations were performed for **{M4}**-CNT systems differing for the direction of the spin magnetic moment of the four magnetic atoms in the complex: aligned parallel (up) or antiparallel (down) to an arbitrary direction. We find that the spin configuration with lowest total energy (ground state) has total spin $S_{tot}^z = 0$ for both isolated[10] and grafted molecules, and for both complexes. The ground state is labelled up-up-down-down (*uudd*) referring to the relative alignment of the four M ions. The M ions connected to the same kind of ligand are almost equivalent, as they face a similar chemical environment. In our notation, the pairs of quasi-equivalent ions are M1/M2 and M3/M4. The ground state presents an

antiferromagnetic (AFM) coupling between non-equivalent M ions (M1/M3, and M2/M4), and a ferromagnetic (FM) coupling between the equivalent pairs (M1/M2 and M3/M4).

The total energy of the investigated spin configurations for the fully relaxed **{Mn$_4$}**-CNT and **{Co$_4$}**-CNT are reported in Tables S1 and S2, together with the magnetization of the four M atoms. As in the free-standing case,[10] the absolute values of the magnetic moments of the two not equivalent pairs of magnetic atoms are slightly different. However, the molecules maintain a total spin $S_{tot}^z \sim 0$ in the AFM configurations, due to the spin polarization of the ligands, which is more relevant in **{Co$_4$}**.

Config.	ΔE [meV]	μ^{S_1} [μ_B]	μ^{S_2} [μ_B]	μ^{S_3} [μ_B]	μ^{S_4} [μ_B]
uudd	**0.0**	**4.82**	**4.82**	**-4.88**	**-4.87**
uddu	2.2	4.82	-4.82	-4.88	4.87
uduu	3.7	4.82	-4.82	4.88	4.87
uuud	5.1	4.82	4.82	4.88	-4.87
uddd	5.5	4.82	-4.82	-4.88	-4.87
uuuu	8.0	4.83	4.82	4.88	4.87
udud	12.8	4.82	-4.82	4.88	-4.87

Table S1 | Low-energy magnetic configurations for the **{Mn$_4$}**-CNT obtained from periodic boundary conditions DFT+U calculations. The ground state (uudd) is highlighted in bold. We report the total energy with respect to the ground state configuration (ΔE, in meV), and the spin magnetic moment for each ion. The units of the magnetic moment are Bohr magnetons (μ_B). The data refer to the 15 cells PBC calculation.

Config.	ΔE [meV]	μ^{S_1} [μ_B]	μ^{S_2} [μ_B]	μ^{S_3} [μ_B]	μ^{S_4} [μ_B]
uudd	**0.0**	**2.70**	**2.71**	**-2.72**	**-2.73**
dddu	10.0	-2.71	-2.71	2.72	-2.74
udud	10.3	-2.70	2.71	-2.72	2.74
uudu	10.9	2.70	2.71	2.72	-2.73
uddd	14.9	-2.71	2.71	-2.72	-2.74
uuuu	18.1	2.71	2.71	2.73	2.74
uddu	20.3	-2.65	2.79	2.65	-2.79

Table S2 | Low-energy magnetic configurations for the **{Co$_4$}**-CNT obtained from periodic boundary conditions DFT+U calculations. The ground state (uudd) is highlighted in bold. We report the total energy with respect to the ground state configuration (ΔE, in meV), and the spin

magnetic moment for each magnetic ion. The units of the magnetic moment are Bohr magnetons (μ_B). The data refer to the 15 cells PBC calculation.

b) {M$_4$}- CNT electronic band structure

All the hybrid {M$_4$}-CNT-systems we modelled are metallic, as illustrated by their electronic band structure (Fig. S2). The {M$_4$} complex does not perturb much the electronic structure of the nanotube in the vicinity of the Fermi energy, indicating that the interaction between nanotube and molecule is weak and explaining why the magnetic properties of the {M$_4$} complex are preserved after bonding to the nanotube. The weak interaction between tube and molecule only causes minor changes in the band structure of the other explored magnetic configurations (not shown). The band structure of the two systems looks very similar, featuring the dispersing bands of CNT (5,5) that are slightly spin polarised and dispersionless (flat) bands whose spin polarisation is larger. These bands that lie above the Fermi level (at ~0.5 eV for {Mn$_4$} and ~0.3 eV for {Co$_4$} in the LDA+U calculation – on the left) correspond to energy levels localised on the {M$_4$} complex. In the calculation with SOC (right) the bands show the same properties apart for a shift of the dispersionless bands toward the Fermi level (for both occupied and empty states) due to the absence of the Hubbard U correction that accounts for the electronic correlation.
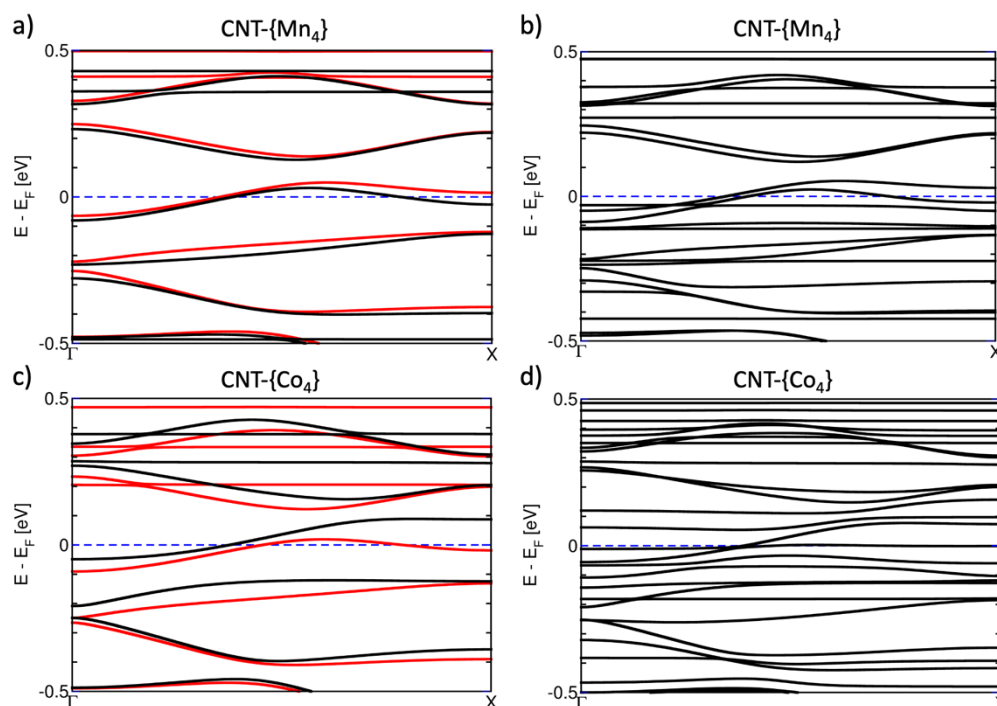

Figure S2 | Electronic band structure of a CNT functionalised with a {Mn$_4$} or {Co$_4$} complex computed in the LDA+U approximation (red: majority spins, black: minority spins, panels a and c), or explicitly including SOC (panel b and d). Flat bands in the electronic structure correspond to the energy levels of the complex. The Fermi level is indicated with a dashed blue line.

2) Open system simulations

a) LDA+U: charge transfer between molecule and tube and localized magnetic moments

Charge transfer was computed in the open system set up. Regardless of the spin configuration, the **{Mn₄}** complex always *withdraws* electron charge from the CNT. In the ground state *uudd* configuration the dangling C in the CNT donates 0.08 electrons while the electronic charge transferred from the other eight C atoms near the -CO₂¯ group (highlighted in yellow in Fig. S3) is 0.1 electrons, for a total of 0.18 electrons donated by the atoms surrounding the monovacancy.

The charge transfer is different for majority and minority spin electronic charge leading to a small magnetic moment of the molecule ($\mu_{\{Mn4\}}$ = -0.006 μ_B) in the ground state configuration, differently from the free-standing case where it was exactly zero. An induced spin polarization is found on the CNT giving $\mu_{\{CNT\}}$ = -0.025 μ_B in the cell. The associated spin density is delocalised over the whole CNT as shown in Fig. 1 of the main manuscript. The C acting as linking site retains a magnetic moment of -0.021 μ_B while the other eight C atoms belonging to the defect site have a total magnetic moment of -0.004 μ_B. Even though the induced spin polarisation is most important at the functionalized vacancy site, the effect is long ranged and allows for a correlation among the spin state of various molecules grafted to the tube.

In **{Co₄}**-CNT ground state the charge transfer from the linking C to the molecule amounts to 0.13 electrons, larger than in **{Mn₄}**-CNT while for the other eight C atoms near the -CO₂¯ group it is 0.03 electrons, i.e. smaller than in the other system. The linking C has an induced magnetic moment of 0.084 μ_B in **{Co₄}**-CNT which is larger, in modulus, than the value found in **{Mn₄}**-CNT. On the other hand, the sum of the magnetic moments of the other eight atoms forming the defect in the CNT is 0.006 μ_B in **{Co₄}**-CNT. The magnetic moment on the molecule is 0.021 μ_B while the net spin polarization induced on the portion of the CNT in the unit cell is 0.117 μ_B i.e. larger than the other compound ($\mu_{\{CNT\}}$ = −0.03 μ_B).

The percentage of the magnetic moment of the C atoms of the CNT in the cell which is localized on the C atoms of the defect at the linking site (linking C + 8 C atoms) is 76% for **{Co₄}**-CNT and 95% for **{Mn₄}**-CNT.
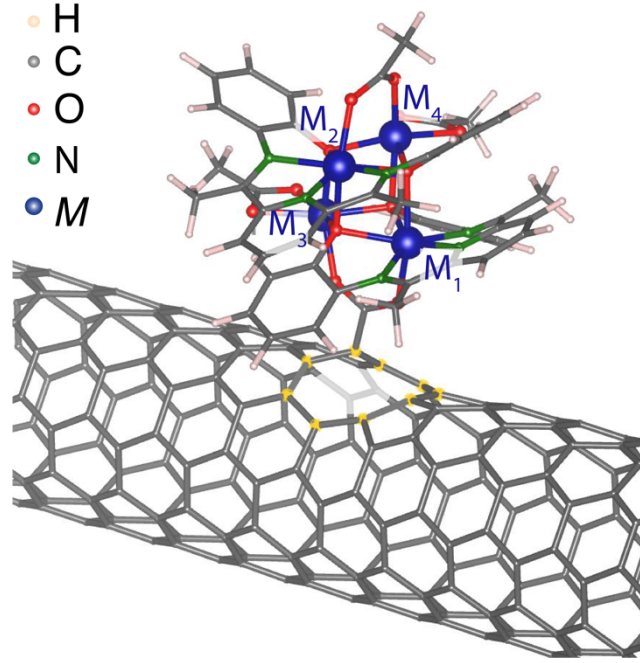
Figure S3 | Linking of the molecule to the CNT. Color code: C - grey, O - red, N - green, Mn/Co - blue. The atoms surrounding the mono-vacancy site where the molecule is grafted to the tube are highlighted in yellow.

b) SOC: Orbital moment on the CNT-{M₄} hybrid systems

The magnetic moments and orbital angular moments on the individual magnetic sites computed for the open system with SOC and without Hubbard correction are given Table S3. The data refer to the ground-state (uudd) configuration. We note a slight reduction of the magnetic moments compared to the calculation with Hubbard correction and without SOC (Table S4): approximately 0.25 μ_B for **{Co₄}**-CNT and 0.15 μ_B for **{Mn₄}**-CNT. The orbital angular moments are finite in **{Co₄}** due to the 3d^7 atomic configuration and are almost negligible in **{Mn₄}** due to the half filling of the 3d shell.

SOC	μ^S_1 [μ_B]	μ^S_2 [μ_B]	μ^S_3 [μ_B]	μ^S_4 [μ_B]	μ^L_1 [μ_B]	μ^L_2 [μ_B]	μ^L_3 [μ_B]	μ^L_4 [μ_B]
{Mn₄}	4.55	4.55	-4.65	-4.61	0.06	0.06	0.07	0.07
{Co₄}	2.56	2.54	-2.60	-2.55	0.16	0.14	0.18	0.25

Table S3 | Magnetic moments and orbital angular moments on the individual magnetic sites of **{Mn₄}**-CNT and **{Co₄}**-CNT computed from first-principles in the open-system set-up with SOC.

LDA+U	μ^S_1 [μ_B]	μ^S_2 [μ_B]	μ^S_3 [μ_B]	μ^S_4 [μ_B]	$\mu^S_{Molecule}$
{Mn₄ }	4.82	4.82	-4.88	-4.87	-0.031
{Co₄}	2.71	2.70	-2.73	-2.72	0.138

Table S4 | Magnetic moments on the individual magnetic sites in **{Mn₄}**-CNT and **{Co₄}**-CNT and residual magnetic moment of the whole **{Mn₄}** and **{Co₄}** molecules computed from first-principles in the open-system set-up with LDA+U.

SI-3 Raman spectrum of the {Mn$_4$} functionalised CNT device

The Raman spectrum shows a metallic tube according to the strong broadening of the $G^{(-)}$-mode[11]; resonance behaviour and position of $G^{(-)}$ and of the TO+ZA combination mode[12] allow for an assignment to the family $2n + m = 30$ (where (n, m) is the CNT chiral index) and the absence of the TO peak suggests a zigzag (15,0) CNT, where the TO mode is Raman-inactive.
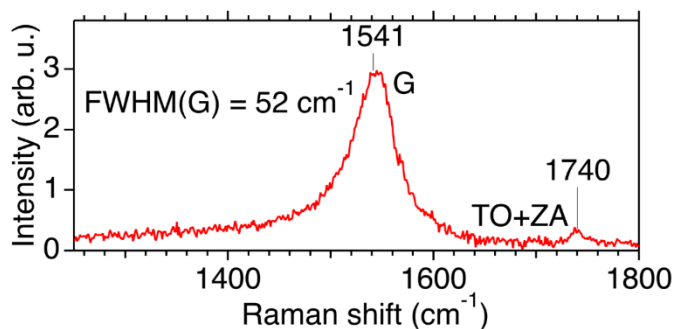

Figure S4 | Raman spectrum of the {Mn$_4$} functionalised CNT device. Shape and position of the $G^{(-)}$-mode and the TO+ZA combination mode in combination with the absence of the TO peak suggest a (15,0) zigzag-CNT.[13]

SI-4 Histogram of the derivative of the direct current data

Since the influence of the slow fluctuations (time scale 10 seconds) on the derivative with (almost) equidistant points with $\Delta t \approx 100$ ms is negligibly small, we use the derivative of the original data to determine the expected standard deviation of the direct current data σ_{direct} which is directly related to the standard deviation of the derivative σ_{deriv} with $\sigma_{direct} = \sigma_{deriv}/\sqrt{2}$.
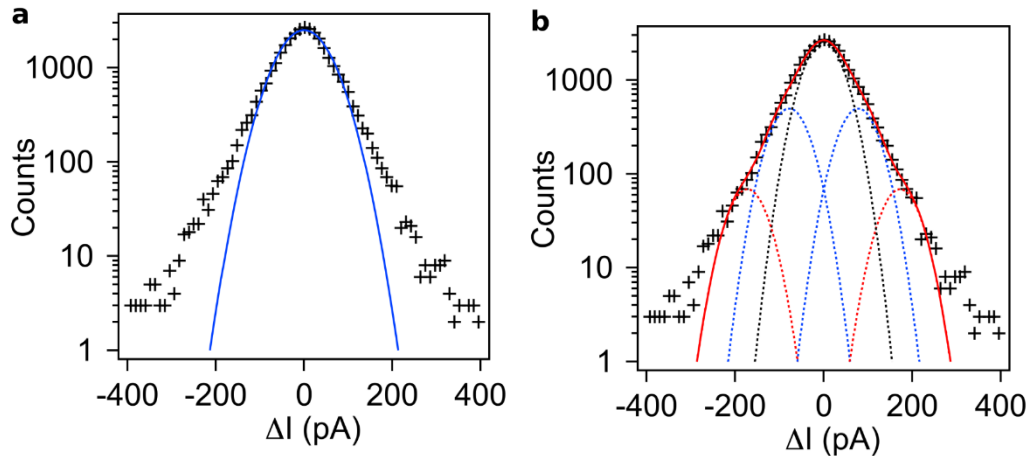

Figure S5 | Histogram of the derivative of the current time traces (black crosses). **a** Fit with a single gaussian peak (blue solid line) **b** Fit with five Gaussian peaks symmetric around 0 (red solid line) revealing the transitions for one current level (blue dotted line) and two current levels (red dotted lines).

Figure S5 compares the fit of the histogram with a single gauss peak with the fit of the histogram with five Gaussian peaks. It is obvious that the data (black crosses) cannot be described with a single gauss peak fit (Fig. S5a, blue solid line). Additional peaks are necessarily symmetric around zero, since the system is clearly neither continuously excited nor relaxed below a ground level. We assume the same standard deviation for all current levels and thus all transitions between levels. Assuming five Gaussian peaks with the second pair of Gaussian peaks (Fig S5b, red dotted lines) have twice the ΔI of the first pair (Fig S5b, blue dotted lines) yields the best fit. The latter constrain does not change the residuum compared to a free position as additional fit parameter. We thus end up with a set of five fit parameters for the five curves: The width, the position of the first pair of Gaussian peaks, the amplitude of the central peak, and the two amplitudes of the two pairs of Gaussian peaks respectively.

We find a standard deviation of $\sigma_{deriv} = 56.4$ (1.3) pA and thus derive a standard deviation of $\sigma_{direct} = 40$ (1) pA for the level broadening in the direct current data after background correction.

SI-5 Theoretical models and results

We model the RTS of the **{Co₄}**- and **{Mn₄}**-functionalised CNT quantum dot by a master equation visualised in figure S6a and b, respectively. The current levels (14 in Fig. 3(a) and three in Figs. 4 and 5(b) in the main paper) correspond to energies with equidistant spacing $\Delta\varepsilon$. We assume that each complex can be excited just once by this amount of energy. For level 0, all K complexes are in their ground state. Each excitation of the molecules attached to the CNT leads to an increase of the level number by one. The main difference between the **{Co₄}** and the **{Mn₄}** systems is how the excitation by energy $\Delta\varepsilon$ is distributed among the grafted complexes. This strongly affects the different transition rates between the levels and, thus, the RTS.

For the **{Co₄}**-system, each excitation is localised at one complex only, i.e. the complexes are excited independently of each other. For $K = 70$ **{Co₄}** complexes there are $K = 70$ possibilities to choose the first complex to be excited (transition from level 0 to level 1) and $K - 1 = 69$ possibilities to choose the second (transition from level 1 to level 2).

For the relaxation from level 1 to level 0, there is no choice but one has to pick the given excited molecule, while for relaxation from level 2 to level 1 two excited molecules are available. In addition to these combinatory factors, there is a Boltzmann factor $r = e^{-\beta\Delta\varepsilon}$ for the excitation relative to the relaxation. The rate Γ sets the overall time scale. This leads to the transition rates depicted in Fig. S6a.
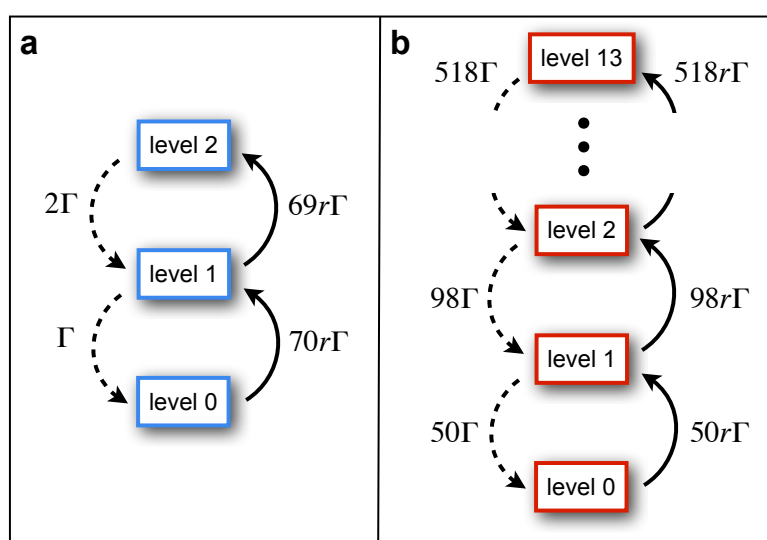

Figure S6 | Sketch of the current levels and the transition rates. a, the **{Co₄}**- and **b,** the **{Mn₄}**-functionalised CNT-quantum-dot device with transitions rate Γ and a Boltzmann factor r. Dashed lines indicate the counted transitions.

For the {Mn₄}-system, we assume *collective* excitations involving *all* $K = 50$ {Mn₄} complexes. The excited states of the full system are coherent superpositions of the excitations of individual complexes. Beginning from the lowest level $|\psi_0\rangle = |0,0,0,\dots,0\rangle$ with each complex in its ground state 0, we construct the states for the higher levels by applying the bosonic operator $\sum_{k=1}^{K} a_k^\dagger$, where $a_k^\dagger$ excites complex k (but only if it is in its ground state), and by normalizing the state afterwards. We obtain

$$|\psi_n\rangle = \frac{1}{\sqrt{\binom{K}{n}}} \left(\sum_{k=1}^{K} a_k^\dagger \right)^n |0,0,0,\dots,0\rangle, \tag{4}$$

which leads to the matrix elements

$$\left| \langle \psi_{n+1} | \sum_{k=1}^{K} a_k^\dagger | \psi_n \rangle \right|^2 = (K - n)(n + 1)$$

and, thus, to the rates depicted in Fig. S6b.

To calculate the factorial cumulants

$$C_{F,m}(\Delta t) = \langle\langle N(N-1) \dots (N - m + 1) \rangle\rangle = \partial_z^m \ln M_F(z, \Delta t)|_{z=0}$$

for the {Co₄}-functionalised CNT quantum dot (and similar for {Mn₄}) assuming K {Co₄} complexes, we write the master equation in the N-resolved form

$$\dot{P}_{N,0}(\Delta t) = -Kr\Gamma P_{N,0}(\Delta t) + P_{N-1,0}(\Delta t), \tag{5}$$

$$\dot{P}_{N,1}(\Delta t) = Kr\Gamma P_{N,0}(\Delta t) - (1 + (K - 1)r)\Gamma P_{N,1}(\Delta t) + 2\Gamma P_{N-1,2}(\Delta t), \tag{6}$$

$$\dot{P}_{N,2}(\Delta t) = (K - 1)r\Gamma P_{N,1}(\Delta t) - 2\Gamma P_{N,2}(\Delta t). \tag{7}$$

Here, $P_{N,n}(\Delta t)$ is the probability that N transitions have occurred and the system is in level n at the end of the time interval Δt. After a z-transform,[14-15] we obtain the generating function $M_F(z, \Delta t) = \vec{e}^T exp[\mathbf{W}_{z+1} \Delta t] \vec{P}_{stat}$ with $\vec{e}^T = (1,1,1)$ and the stationary density matrix given by $\mathbf{W}_1 \vec{P}_{stat} = (0,0,0)^T$ and $\vec{e}^T \vec{P}_{stat} = 1$. The matrix $\mathbf{W}_z$ is given by

$$\mathbf{W}_z = \begin{pmatrix} -Kr & z & 0 \\ Kr & -1 - (K-1)r & 2z \\ 0 & (K-1)r & -2 \end{pmatrix} \Gamma. \tag{8}$$

For the simulations presented in Fig. 7 of the main paper, the two parameters Γ and r have been determined such that the simulation reproduces the first factorial cumulant $C_{F,1}(10s)$ and the ratio $P_{occ}(\psi_1)/P_{occ}(\psi_0)$ of the occupations of level 1 and 0 exactly. Higher-order factorial cumulants and the probability of the higher levels are then a result of the simulation without any further fitting parameter.

In case of a system in which the counted transitions happen independently from each other, the sign of the m-th factorial cumulant must be $(-1)^{m-1}$ for all Δt.[16,15,17] This is, indeed, the case for independent two-level fluctuators, in accordance with the {Co₄}-data (blue curves in Fig. 7(b)-(d) of the main paper). The {Mn₄}-data (red curves in Fig. 7(b)-(d) of the main paper)

show a different behaviour, i.e. they cannot be modelled by independent two-level fluctuators. The assumption of coherent superpositions of the excitations, on the other hand, can reproduce the data.

For completeness, we check yet another model for the **{Mn$_4$}**-data. Let us assume local excitations of independent *three-level* fluctuators, i.e. each complex can accommodate *two* excitations which, by chance, happen to have the same excitation energy. In Fig. S7, we depicted the results for this model (Fig. S7a). The additional parameter $\tilde{\Gamma}$ is determined such that the simulation reproduces $C_{F,2}(10s)$ exactly. Indeed, the cumulants observed in the experiment can be reproduced by the simulation (Fig. S7c, d, and e). However, the occupation probabilities P_{occ} are not recovered (Fig. S7b). Similar as for the two-level fluctuators, the combinatorial factors associated with the degeneracy of the levels strongly suppress the occupation probabilities in comparison to ones extracted from the measurements. Furthermore, very different values of $\tilde{\Gamma}$ and Γ would be needed without any physical justification. We, thus, conclude that only the model assuming coherent superpositions can reproduce the measured data.
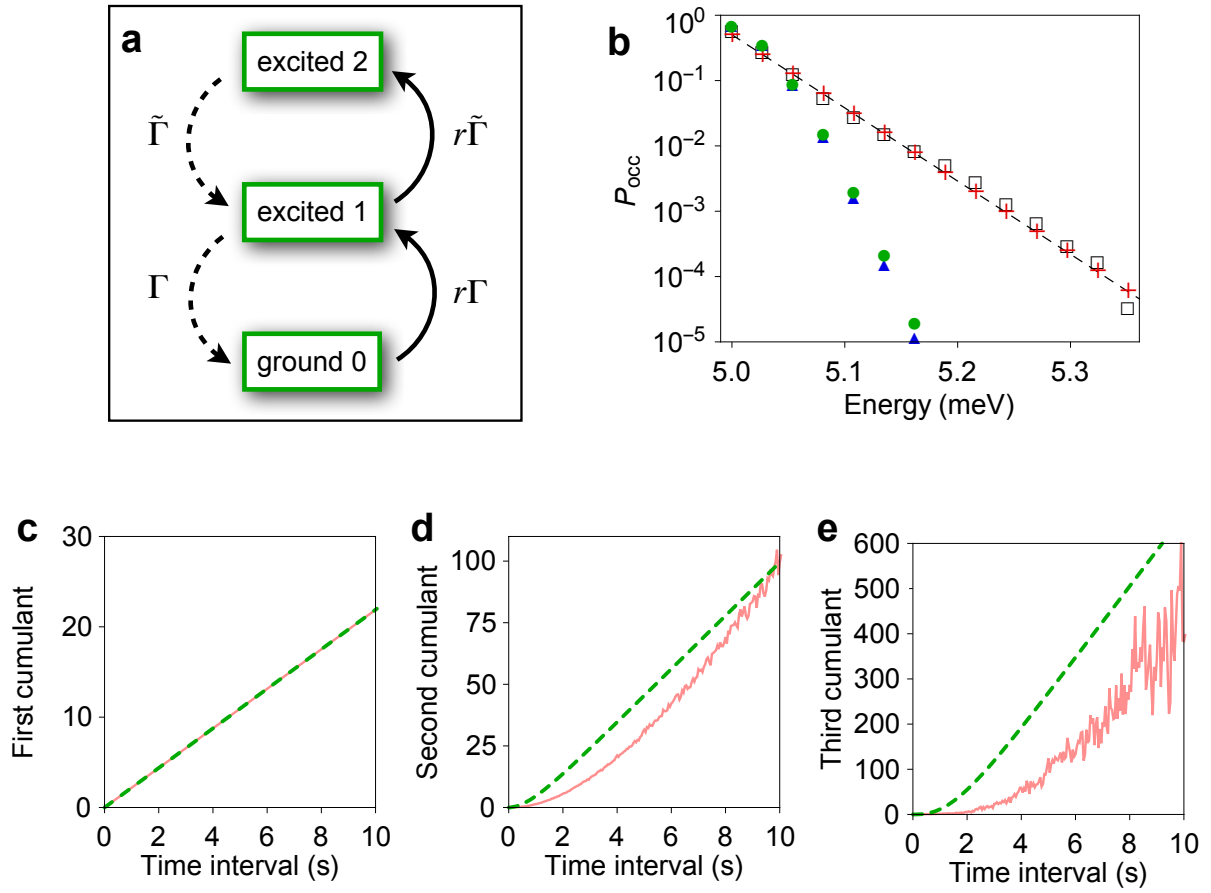
Figure S7 | Sketch and modelling of a three-level fluctuator. a, States and possible transitions of a three-level fluctuator. **b,** Occupation probability on a logarithmic scale for the different levels for the original data (black squares), and for models assuming $K = 50$ independent two-level fluctuators (blue triangles), $K = 50$ independent three-level fluctuators (green dots), and $K = 50$ coherently coupled two level fluctuators (red crosses). **c, d, e,** First, second, and third factorial cumulant as extracted from the measurements (red solid line) and a simulation assuming $K = 50$ independent three-level fluctuators (green dashed line) with $r = 0.01$, $\Gamma = 1.25\ s^{-1}$, and $\tilde{\Gamma} = 316.99\ s^{-1}$.

References

1.   Soler, J. M.; Artacho, E.; Gale, J. D.; García, A.; Junquera, J.; Ordejón, P.; Sánchez-Portal, D., The Siesta Method Forab Initio Order-N Materials Simulation. *J. Phys.: Condens. Matter* **2002,** *14*, 2745-2779, DOI: 10.1088/0953-8984/14/11/302.

2.   García, A.; Papior, N.; Akhtar, A.; Artacho, E.; Blum, V.; Bosoni, E.; Brandimarte, P.; Brandbyge, M.; Cerdá, J. I.; Corsetti, F.; Cuadrado, R.; Dikan, V.; Ferrer, J.; Gale, J.; García-Fernández, P.; García-Suárez, V. M.; García, S.; Huhs, G.; Illera, S.; Korytár, R.*et al.*, Siesta: Recent Developments and Applications. *Journal of Chemical Physics* **2020,** *152*, 204108, DOI: 10.1063/5.0005077.

3.   Zanolli, Z.; Charlier, J. C., Defective Carbon Nanotubes for Single-Molecule Sensing. *Phys Rev B* **2009,** *80*, 155447, DOI: 10.1103/PhysRevB.80.155447.

4.   Zanolli, Z.; Charlier, J. C., Single-Molecule Sensing Using Carbon Nanotubes Decorated with Magnetic Clusters. *ACS Nano* **2012,** *6*, 10786-10791, DOI: 10.1021/nn304111a.

5.   Dudarev, S. L.; Botton, G. A.; Savrasov, S. Y.; Humphreys, C. J.; Sutton, A. P., Electron-Energy-Loss Spectra and the Structural Stability of Nickel Oxide: An LSDA+U Study. *Phys. Rev. B* **1998,** *57*, 1505-1509, DOI: 10.1103/PhysRevB.57.1505.

6.   Kampert, E.; Janssen, F. F. B. J.; Boukhvalov, D. W.; Russscher, J. C.; Smits, J. M. M.; de Gelder, R.; de Bruin, B.; Christianen, P. C. M.; Zeitler, U.; Katsnelson, M. I.; Maan, J. C.; Rowan, A. E., Ligand-Controlled Magnetic Interactions in Mn_4 Clusters. *Inorganic Chemistry* **2009,** *48*, 11903-11908, DOI: 10.1021/ic901930w.

7.   Cuadrado, R.; Cerdá, J. I., Fully Relativistic Pseudopotential Formalism under an Atomic Orbital Basis: Spin–Orbit Splittings and Magnetic Anisotropies. *J. Phys.: Condens. Matter* **2012,** *24*, 086005, DOI: 10.1088/0953-8984/24/8/086005.

8.   Brandbyge, M.; Mozos, J.-L.; Ordejón, P.; Taylor, J.; Stokbro, K., Density-Functional Method for Nonequilibrium Electron Transport. *Phys. Rev. B* **2002,** *65*, 165401, DOI: 10.1103/PhysRevB.65.165401.

9.   Papior, N.; Lorente, N.; Frederiksen, T.; García, A.; Brandbyge, M., Improvements on Non-Equilibrium and Transport Green Function Techniques: The Next-Generation Transiesta. *Comput Phys Commun* **2017,** *212*, 8-24, DOI: 10.1016/j.cpc.2016.09.022.

10.   Achilli, S.; Besson, C.; He, X.; Ordejòn, P.; Meyer, C.; Zanolli, Z., Magnetic Properties of Coordination Clusters with {Mn_4} and {Co_4} Antiferromagnetic Cores. *Phys. Chem. Chem. Phys.* **2022,** *24*, 3780-3787, DOI: 10.1039/D1CP03904K.

11.   Piscanec, S.; Lazzeri, M.; Robertson, J.; Ferrari, A. C.; Mauri, F., Optical Phonons in Carbon Nanotubes: Kohn Anomalies, Peierls Distortions, and Dynamic Effects. *Phys Rev B* **2007,** *75*, 035427, DOI: 10.1103/PhysRevB.75.035427.

12.   Vierck, A.; Gannott, F.; Schweiger, M.; Zaumseil, J.; Maultzsch, J., ZA-Derived Phonons in the Raman Spectra of Single-Walled Carbon Nanotubes. *Carbon* **2017,** *117*, 360-366, DOI: 10.1016/j.carbon.2017.02.101.

13.   Reich, S.; Thomsen, C.; Maultzsch, J., *Carbon Nanotubes: Basic Concepts and Physical Properties*. Wiley-VCH: Berlin, 2004.

14.   Johnson, N. L.; Kemp, A. W.; Kotz, S., *Univariate Discrete Distributions*. 3rd ed.; John Wiley & Sons, Inc.: Hoboken, 2005.

15.   Stegmann, P.; Sothmann, B.; Hucht, A.; König, J., Detection of Interactions Via Generalized Factorial Cumulants in Systems in and out of Equilibrium. *Phys Rev B* **2015,** *92*, 155413, DOI: 10.1103/PhysRevB.92.155413.

16.   Kambly, D.; Flindt, C.; Büttiker, M., Factorial Cumulants Reveal Interactions in Counting Statistics. *Phys Rev B* **2011,** *83*, 075432, DOI: 10.1103/PhysRevB.83.075432.

17.   Stegmann, P.; König, J., Short-Time Counting Statistics of Charge Transfer in Coulomb-Blockade Systems. *Phys. Rev. B* **2016,** *94*, 125433, DOI: 10.1103/PhysRevB.94.125433.